Solar Energy 307 (2026) 114327

Contents lists available at ScienceDirect

Solar Energy

journal homepage: www.elsevier.com/locate/solener

Bionic marine seaweed evaporator for effective seawater desalination

Xinzhe Liu [a], Ting Chen [b,*], Tiezhi Wang [a], Jinliang Xu [a], Ying He [a], Guohua Liu [a,c,**]

[a] Beijing Key Laboratory of Multiphase Flow and Heat Transfer for Low Grade Energy Utilization, North China Electric Power University, Beijing 102206, PR China
[b] School of Optoelectronic Materials and Technology, Jianghan University, Wuhan 430056, PR China
[c] Key Laboratory of Power Station Energy Transfer Conversion and System (North China Electric Power University), Ministry of Education, Beijing 102206, PR China

ARTICLE INFO

Keywords:
Marine seeding
Seawater desalination
Salt resistance
Freshwater collection

ABSTRACT

This study proposes the "marine seeding" concept and develops an interfacial evaporator based on it for efficient seawater desalination. polyvinyl alcohol and graphene oxide are uniformly coated on cotton fibers to harden them, and self-floating is achieved with the help of polystyrene foam. The porous interconnected structure of the PVA/GO/cotton composite can shorten the water molecule transport path and achieve rapid water transport to meet the water supply demand during the evaporation process. And the gradient heat distribution formed on the evaporator surface due to photothermal conversion will drive the natural convection of brine, accelerate the diffusion of salt ions into the bulk solution, and effectively avoid surface salt accumulation. The marine seeding evaporator can reach a seawater evaporation rate as high as 2.451 $kg{\cdot}m^{-2}{\cdot}h^{-1}$ and shows no salt crystallization during 6 days long-term test. Moreover, the reduction in the evaporation enthalpy of water in the evaporator and the changes in water state have been confirmed through dark evaporation tests, Differential Scanning Calorimetry, and Raman spectroscopy. And the freshwater collection device assembled with the evaporator has a daily freshwater collection of up to 10.18 $L{\cdot}m^{-2}$. This research paves the way for a more efficient and sustainable seawater desalination solution.

1. Introduction

In the 21st century, the global water crisis has reached an unprecedented level of severity [1,2,3]. With the exponential growth of the world's population, which is expected to approach 10 billion by 2050, and the rapid expansion of industrial activities, the demand for freshwater has increased sharply [4,5]. At the same time, climate change has exacerbated water scarcity in many regions, leading to problems such as droughts, reduced river flows, and the depletion of groundwater resources [6,7]. Current estimates from recent United Nations reports (including joint publications by WHO and UNICEF) indicate that over 2.4 billion people lack access to safely managed drinking water, and this situation is expected to deteriorate further [8,9]. Seawater desalination has become a key strategy for addressing this water shortage problem. The Earth's oceans, covering approximately 71 % of the planet's surface, represent an almost inexhaustible source of water [10]. Through the conversion of seawater into freshwater, seawater desalination technology can provide a reliable and stable water source for domestic, agricultural, and industrial use [11,12]. This is particularly important for arid coastal regions and small island countries facing severe water shortages. However, the successful large-scale application of seawater desalination technology depends on the development of efficient and sustainable technologies.

Current seawater desalination technologies can be roughly divided into membrane-based processes and thermal processes [13,14]. Membrane-based methods, such as reverse osmosis (RO), are widely used because of their relatively higher efficiency and lower energy consumption compared with some thermal processes [15,16]. In a reverse osmosis system, seawater is forced to pass through a semi-permeable membrane under high pressure. Water molecules can permeate through it, while salt ions are retained. However, reverse osmosis technology has some limitations. The high operating pressure required leads to a large amount of energy consumption, and the membrane is prone to contamination by organic matter, microorganisms, and scaling salts [17,18]. This will shorten the service life of the membrane and increase maintenance costs. Thermal seawater desalination processes, including multi-stage flash (MSF) distillation and multi-effect distillation (MED), rely on the evaporation and

* Corresponding author.
** Corresponding author at: Beijing Key Laboratory of Multiphase Flow and Heat Transfer for Low Grade Energy Utilization, North China Electric Power University, Beijing 102206, PR China.
E-mail addresses: chenting631@163.com (T. Chen), liuguohua126@126.com (G. Liu).

https://doi.org/10.1016/j.solener.2026.114327
Received 9 October 2025; Received in revised form 2 January 2026; Accepted 8 January 2026
Available online 12 January 2026
0038-092X/© 2026 International Solar Energy Society. Published by Elsevier Ltd. All rights are reserved, including those for text and data mining, AI training, and similar technologies.

condensation of seawater [19,20]. In multi-stage flash distillation, seawater is heated in a series of chambers with gradually decreasing pressure, causing it to flash into steam, which is then condensed into fresh water. On the other hand, multi-effect distillation makes use of the latent heat of vaporization of one effect to heat the seawater in the next effect, thus improving energy efficiency. Nevertheless, these thermal processes are energy-intensive, usually requiring a large quantity of fossil fuels, and they generate a significant amount of greenhouse gas emissions [21,22,23]. Additionally, they are capital-intensive with high construction and operation costs, making it difficult for many developing regions to adopt them.

Interfacial evaporation technology has recently emerged as a promising alternative for seawater desalination [24,25]. This technology is based on the principle of selectively heating the water–air interface to promote evaporation while minimizing the heat loss to the bulk solution. It has several potential advantages. For instance, it can utilize low-grade heat energy, enabling it to make use of renewable energy sources such as solar energy, and the system configuration is relatively simple. In recent years, significant progress has been made in the development of interfacial evaporation materials and structures [26,27,28]. For example, the use of hydrophilic porous materials, such as cellulose-based materials and metal–organic frameworks (MOFs), has been explored to enhance the transport of water to the evaporation interface [29,30]. Nanocomposites containing graphene or carbon nanotubes have also been studied due to their excellent thermal conductivity, which can improve the heat transfer efficiency at the interface [31,32]. However, interfacial evaporation technology still faces some challenges. One of the major issues is the accumulation and fouling of salts at the evaporation interface. As seawater evaporates, salt ions concentrate at the interface, leading to the formation of salt crystals [33,34]. These crystals may block the pores of the evaporation materials, reduce the evaporation efficiency, and eventually damage the equipment. Another challenge is that the evaporation rate is relatively low compared with the theoretical potential. Factors such as inefficient water supply to the evaporation interface, limited heat transfer, and suboptimal material properties all contribute to this problem. In addition, considering factors such as corrosion, biofouling, and variable environmental conditions in the actual marine environment, the long-term stability of interfacial evaporation systems remains to be fully addressed.

In this study, we propose a novel interfacial evaporator inspired by the concept of “marine seeding” to overcome the challenges faced by existing seawater desalination technologies. This concept is inspired by the natural structure and function of seagrasses in the ocean. Seagrasses can efficiently absorb and transport water while resisting the intrusion of salt. We have designed a composite structure consisting of polyvinyl alcohol (PVA), graphene oxide (GO), and cotton fibers. PVA and GO are uniformly coated on the cotton fibers. The porous interconnected structure of the PVA/graphene oxide/cotton composite can shorten the water molecule transport path and achieve rapid water transport to meet the water supply demand during the evaporation process; the gradient heat distribution formed on the evaporator surface due to photothermal conversion will drive the natural convection of brine, accelerate the diffusion of salt ions into the bulk solution, and effectively avoid surface salt accumulation. To enable the evaporator to self-float on the sea surface, we have incorporated polystyrene foam into the design. This not only allows for the easy deployment of the evaporator in the marine environment but also reduces the need for complex support structures. Our experimental results show that the marine seeding interfacial evaporator can achieve an evaporation rate as high as 2.451 $kg{\cdot}m^{-2}{\cdot}h^{-1}$, and no salt crystallization was observed during the long-term test lasting for 6 days. The freshwater collection device integrated with the evaporator demonstrates the daily freshwater collection 10.18 $L{\cdot}m^{-2}$, and the collected freshwater meets the drinking water standards of the World Health Organization. This research represents an important step towards the development of a more efficient, sustainable, and practical seawater desalination solution, which has the potential to be applied in various environments.

2. Materials and methods

2.1. Preparation of materials and solutions

Cotton fibers were selected as the basic framework. Pure and impurity-free natural cotton fibers were used to ensure good water absorption and structural stability. PVA, purchased from Aladdin with CAS number 9002–89-5, was used directly as an analytical reagent. GO was prepared by the modified Hummers method. In a 250 mL round-bottom flask, 1 g of expanded graphite was added first, followed by the injection of 100 mL of a mixture of 98 % sulfuric acid (90 mL) and 85 % phosphoric acid (10 mL) at a volume ratio of 9:1. The mixture was stirred at 300 r/min for 1 h. Under ice-bath stirring, 6 g of potassium permanganate was added portion-by-portion within 30 min while controlling the temperature below 20 °C. Subsequently, the mixture was stirred in a 45 °C water bath at 250 r/min for 12 h. After cooling, the reaction solution was transferred to a 500 mL beaker, and 80 mL of a 5 wt% hydrogen peroxide solution and 20 mL of 37 % hydrochloric acid solution were added in sequence. The mixture was stirred at 250 r/min for 1 h. Then, the solution was centrifuged at 8000 r/min for 15 min. The supernatant was discarded, and the precipitate was resuspended in deionized water and recentrifuged. This washing process was repeated 5 times until the pH of the supernatant was nearly neutral. Finally, the precipitate was freeze-dried at −10 °C and 10 Pa for 24 h, and the obtained GO product was sealed for storage. Polystyrene foam with a density of 30 kg/m^3 was selected. Its low thermal conductivity was approximately 0.03 W/(m·K). Such foam could not only provide sufficient buoyancy but also reduce heat loss, ensuring the stability of the evaporator during evaporation experiments. The pure water used in the evaporation experiments was laboratory-made deionized water, the seawater was real seawater collected from the coast of Qingdao, and brines with different concentrations were prepared by adding sodium chloride to deionized water.

2.2. Assembly of the marine seeding evaporator

10 g PVA was weighed and added to 100 mL deionized water. The mixture was heated and stirred at 80 °C until PVA was completely dissolved, forming a transparent solution. 15 g cotton fibers were immersed in the PVA solution. After being fully infiltrated, they were taken out, with a layer of PVA adhering to the surface of the cotton fibers, which would serve as an adhesive. Subsequently, the PVA-adhered cotton fibers were added to the 30 mL graphene oxide solution (0.5 g/L) so that the graphene oxide sheets were uniformly loaded onto the surface of the cotton fibers by virtue of the viscosity of PVA. Then, the loaded cotton fibers were placed in a vacuum drying oven at 60 °C for 120 min. PVA solidified, making the cotton fibers stiff, and meanwhile, GO adhered firmly. Finally, the cotton fibers loaded with PVA and graphene oxide were fixed onto the polystyrene foam, thus completing the assembly of the marine seeding evaporator.

2.3. Materials characterization

The lamellar structure of graphene oxide and the microstructures of the assembled evaporator were observed using a scanning electron microscope (Hitachi S4800) to verify the successful assembly of the interfacial evaporator. The light absorption properties of graphene oxide and the evaporator were analyzed by a UV–Vis-NIR spectrometer (UV-3600 PLUS). The ion concentrations in solutions before and after evaporation were determined with an inductively coupled plasma mass spectrometer (Thermo Scientific ICAP). The surface temperature variations of the evaporator were measured by a precision infrared thermal imager (Infratec IR5300). The droplet contacts angles of cotton fibers

before and after being loaded with PVA and graphene oxide were characterized using a contact-angle measuring instrument (Dataphysics OCA − 20) to confirm their hydrophilicity.

2.4. Solar steam generation experiment

The indoor evaporation test was carried out systematically using a solar simulator (AbetTech, M−LS Rev B) equipped with an AM1.5 l filter (CEL-PE300-3A). Prior to the test, the parameters of the solar simulator needed to be finely adjusted. By flexibly adjusting its height and precisely controlling the current intensity, the solar irradiance was finally stably adjusted to 1 solar constant, namely 1000 W·m^{-2}, to simulate the real solar illumination environment. During the experiment, a water container filled with sufficient test liquid and the carefully prepared evaporator were placed together on a precision balance (Setra, BL-500S) connected to a computer. The balance recorded mass changes in real − time and accurately at a fixed sampling rate of 1 data point per 5 s. Subsequently, through systematic analysis of these data, the evaporation rate could be accurately calculated. Each test was performed in 3 times, and the mean value was adopted for result analysis. During the test, the indoor temperature was maintained at 30 ± 1 °C, and the relative humidity was maintained at 30 ± 2 %. The evaporation rate was calculated using equation (1):

$$E = \frac{\Delta m}{A \times \Delta t} \tag{1}$$

where E is the evaporation rate with the unit of kg·m^{-2}·h^{-1}; m represents the water mass measured via an electronic balance with the unit of kg; A refers to the effective evaporation area of the evaporator with the unit of m^2; and t is the measurement time interval with the unit of h. The photothermal conversion efficiency was calculated using Eq. (2):

$$\eta = \frac{E \times H}{q \times A} \times 100\% \tag{2}$$

where H is the evaporation enthalpy of water with the unit of J·kg^{-1}; and q is the incident solar irradiance with the unit of W·m^{-2}.

2.5. Numerical simulation

The evaporation process was simulated using the commercial finite-element analysis solver COMSOL Multiphysics 6.2; comprehensive modeling details are provided in Supplementary Note 1.

2.6. Thermodynamic test

The hydrogen-bonding network of water in each specimen was characterized by micro-Raman spectroscopy (λ = 532 nm; LabRAM HR Evolution, Horiba), focusing on the O–H stretching region. The enthalpy of evaporation was quantified using a simultaneous TGA/DSC 1 system (Mettler-Toledo). Prior to measurements, heat-flow calibration and effective heat capacity determination were performed against a sapphire reference to ensure accuracy. Samples (5–10 mg) were hermetically sealed in aluminum crucibles, then heated from 40 to 120 °C at 5 °C·min^{-1} under a 50 mL·min^{-1} nitrogen purge (≥99.99 % purity) to avoid interference from ambient moisture and oxygen.

2.7. Outdoor test

Based on the indoor evaporation test, an integration was carried out. The evaporator used in the indoor experiment was scaled-up and then assembled with a condenser made of acrylic board to obtain an outdoor freshwater collection device. This device was placed on the west side of Teaching Building D at North China Electric Power University (Beijing), with the coordinates of 116°20′24″ E and 40°09′74″ N. The amount of freshwater in the condenser was recorded every 1 h to calculate the freshwater collection rate and the daily freshwater collection volume.

3. Results and discussion

3.1. Concept and preparation of the marine seeding evaporator (MSE)

The marine seeding evaporator's design concept is innovative, inspired by seagrass's unique structure and function. Seagrass uses its stems to build an efficient water absorption and transportation system, which the evaporator cleverly emulates. As can be seen from the concept schematic in Fig. 1a, its operation mode is revealed. By adopting the multi-directional extension of seagrass, it is crafted into a three − dimensional structure, significantly expanding the side area [35]. This breaks through the limitation of traditional evaporators that only rely on top-surface evaporation, making full use of side surface evaporation and greatly increasing the evaporation area, thus laying a structural foundation for high efficiency evaporation [36,37]. In terms of anti-salt performance, the anti-salt schematic in Fig. 1b reveals the key mechanism. The porous interconnected structure of the PVA/GO/cotton composite can shorten the water molecule transport path and achieve rapid water transport to meet the water supply demand during the evaporation process. And the gradient heat distribution formed on the evaporator surface due to photothermal conversion will drive the natural convection of brine, accelerate the diffusion of salt ions into the bulk solution, and effectively avoid surface salt accumulation [38,39,40]. This characteristic overcomes the problems of salt accumulation and scaling in traditional seawater desalination technologies, is of great significance for maintaining the long-term stable evaporation operation, and lays a good foundation for subsequent large-scale applications.

The observation of the microstructure using the scanning electron microscope (SEM) further validates the unique design and excellent performance of the MSE. Fig. 1c shows the SEM image of graphene oxide, clearly revealing its lamellar structure. These lamellar structures not only boost the material's specific surface area but also create optimal conditions for water transport and salt ion exclusion. The cross-sectional SEM image of the evaporator (Fig. 1d) presents a clear three-dimensional structure. A remarkable structural advantage of the MSE lies in its three-dimensional nature, with a cross-sectional thickness of only 0.5 cm. This structural design enables the MSE to fully utilize the side surface for evaporation, significantly increasing the evaporation area. Compared with traditional two-dimensional evaporators, its evaporation efficiency has been substantially improved. From Fig. 1d, it can be observed that PVA and graphene oxide are uniformly loaded on the cotton fibers, and the three components are closely combined to form a stable composite structure. The magnified cross-sectional SEM image in Fig. 1e further reveals the micro-details of the composite structure. The cotton fibers are tightly wrapped by PVA and graphene oxide, forming a smooth and ordered micro-network. This

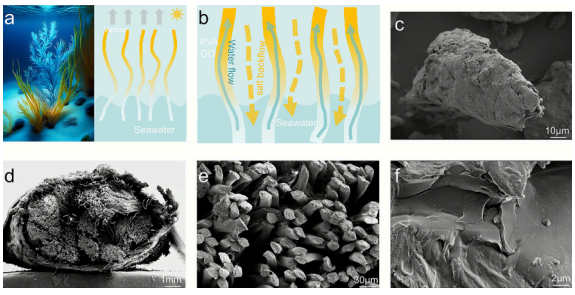


Fig. 1. Concept and Preparation of the Marine Seeding Evaporator (MSE). (a) The marine seeding evaporator concept schematic. (b) The anti-salt schematic of MSE. (c) The SEM image of graphene oxide. (d) The cross-sectional SEM image of the MSE. (e) The magnified cross-sectional SEM image. (f) The SEM image at a scale of 2 μm.

microstructure not only enhances the mechanical strength of the material but also optimizes the water transport path. As an adhesive, PVA effectively connects graphene oxide and cotton fibers, ensuring the structural stability. No obvious channel structure was observed in Fig. 1f, salt ions do not penetrate into the interior of cotton fibers. Instead, water is rapidly transported through the surface tension between cotton fibers, thus achieving salt resistance. [41,42]. The innovation in the concept and preparation of the MSE endows it with numerous advantages in structure and performance.

3.2. Wetting properties and photothermal conversion

Wetting properties are one of the crucial factors for the efficient operation of the evaporator, directly influencing the transportation and evaporation efficiency of water on the material surface. As shown in Fig. 2a and Fig. 2b, the droplet contacts angles of both cotton fibers and the MSE are 0°. This phenomenon indicates that the loading process of PVA and graphene oxide has not impaired the original excellent hydrophilicity of cotton fibers. As the basic framework, the natural hydrophilicity of cotton fibers enables water to infiltrate rapidly and spread on the surface. The addition of PVA and graphene oxide not only maintains this property but also further optimizes the water transportation pathway by forming a stable composite structure. The retention of this hydrophilicity provides a strong guarantee for the MSE to absorb seawater quickly during the seawater desalination process [43]. Seawater can adhere to the surface of the evaporator rapidly, laying the foundation for the subsequent evaporation process. In terms of photothermal conversion performance, Fig. 2c illustrates the spectral absorption of graphene oxide and the MSE. The average spectral absorption of graphene oxide reaches as high as 95.21 %, and that of the MSE is 97.01 %, which fully demonstrates that PVA has no negative impact on the overall spectral absorption capacity during the loading process. This result is of great significance because the photothermal conversion efficiency is closely related to the spectral absorptivity. The three-dimensional structure of cotton fibers plays a vital role here. It increases the scattering and reflection of light within the material, prolongs the interaction path between light and the material, and thus promotes light trapping. More light absorption means that more light energy can be converted into heat energy, providing the energy required for the evaporation of seawater. Compared with traditional planar-structured materials, the three-dimensional structure of the MSE significantly enhances the light utilization efficiency, allowing it to absorb more energy under the same illumination conditions.

The temperature variations of MSE in the dark and illuminated conditions further reveal its unique properties. Fig. 2d shows that in the dark environment, the MSE temperature (19.45 °C) is lower than the ambient temperature (31.33 °C). This phenomenon indicates that MSE

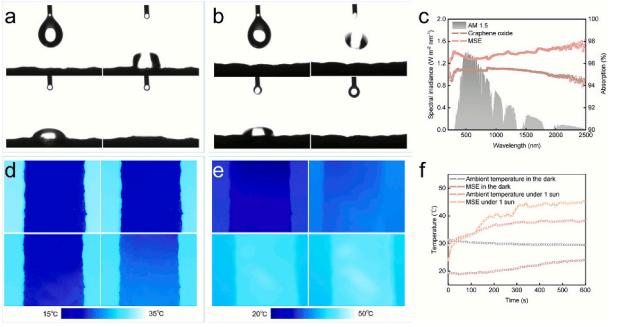


Fig. 2. Wetting Properties and Photothermal Conversion. (a) The droplet contacts angle of cotton fibers. (b) The droplet contacts angle of the MSE. (c) The spectral absorption of graphene oxide. (d) The MSE in the dark. (e) The MSE under 1 sun. (f) The temperature change curve of MSE in the dark and under 1 sun.

can absorb energy from the surrounding environment. This characteristic stems from its special material structure and micro-interface properties, enabling energy exchange between the material and the environment. Although there is no external light source to provide energy in the dark, MSE can draw energy from the environment through heat exchange with it, maintaining a certain temperature difference and creating favorable conditions for water transport and evaporation. This ability to absorb energy from the environment is of great significance in practical applications. Even when the illumination is insufficient, MSE can still maintain a certain operating efficiency. As we can see for Fig. 2e, MSE can rapidly rise to 45.09 °C in an extremely short time, much higher than the ambient temperature (38.18 °C), clearly demonstrating its strong photothermal conversion ability. Under the action of light, graphene oxide absorbs light energy and quickly converts it into heat energy. The heat is rapidly transferred through the composite structure composed of PVA and cotton fibers, promoting the rapid evaporation of water. The temperature-change curve in Fig. 2f intuitively presents this process. In the dark conditions, the temperature of MSE gradually approaches the ambient temperature, while under 1 sun illumination, the temperature rises rapidly and reaches a high level in a short time and then remains stable. This rapid temperature response and high-efficiency photothermal conversion ability endows MSE with significant advantages in seawater desalination applications.

3.3. Seawater desalination and long-term stability

Seawater desalination, as a core strategy to address the global shortage of fresh water resources, poses extremely stringent requirements for the performance and stability of evaporators. Fig. 3a shows the optical photograph of the indoor evaporation test. From the evaporation rate data of MSE for pure water in the dark and under 1 sun illumination in Fig. 3b, it can be seen that illumination has a significant impact on its evaporation efficiency. In the dark environment, MSE achieves an evaporation rate of 0.603 $kg{\cdot}m^{-2}{\cdot}h^{-1}$ through its energy interaction mechanism with the surrounding environment. Under 1 sun, its evaporation rate soars to 2.687 $kg{\cdot}m^{-2}{\cdot}h^{-1}$, clearly demonstrating the strong evaporation capacity of MSE driven by photothermal conversion. This indicates that illumination can provide an additional and efficient energy source for water evaporation. When dealing with brines of different concentrations, MSE exhibits unique performance characteristics. As can be seen from Fig. 3c, when treating seawater, the evaporation rate of MSE can reach 2.453 $kg{\cdot}m^{-2}{\cdot}h^{-1}$. As the brine concentration increases, for example, when treating 5 wt% brine, the evaporation rate slightly drops to 2.369 $kg{\cdot}m^{-2}{\cdot}h^{-1}$; when treating 15 wt% brine, the rate is 2.121 $kg{\cdot}m^{-2}{\cdot}h^{-1}$; even when treating high-concentration brine as high as 25 wt%, the evaporation rate of MSE still remains at 1.946 $kg{\cdot}m^{-2}{\cdot}h^{-1}$. This means that the photothermal conversion efficiencies of the MSE are 98.64 % (pure water), 90.05 % (seawater), 86.97 % (5 wt% brine), 77.86 % (15 wt% brine), and 71.44 % (25 wt% brine), respectively. This phenomenon shows that although the increase in brine concentration will pose certain obstacles to the evaporation process, MSE can overcome this resistance to a large extent due to its innovative structural design and material properties.

In the practical application scenarios of seawater desalination, the long-term stability of the evaporator is a key indicator for evaluating its performance. The results of the 8 h continuous seawater evaporation test and the 6 days continuous seawater evaporation test shown in Fig. 3d and Fig. 3e respectively provide strong evidence for the stability assessment of MSE. During the 8 h continuous test, the evaporation rate of MSE stably remained at 2.454 $kg{\cdot}m^{-2}{\cdot}h^{-1}$, which preliminarily demonstrates its ability to operate stably in a short period and continuously and efficiently carry out seawater desalination operations. More importantly, during the 6 days long-term test, the evaporation rate of MSE always remained stable at around 2.451 $kg{\cdot}m^{-2}{\cdot}h^{-1}$, showing excellent long-term stability. Combined with the images of the 6 days operation process presented in Fig. 3f, no salt crystallization occurred on

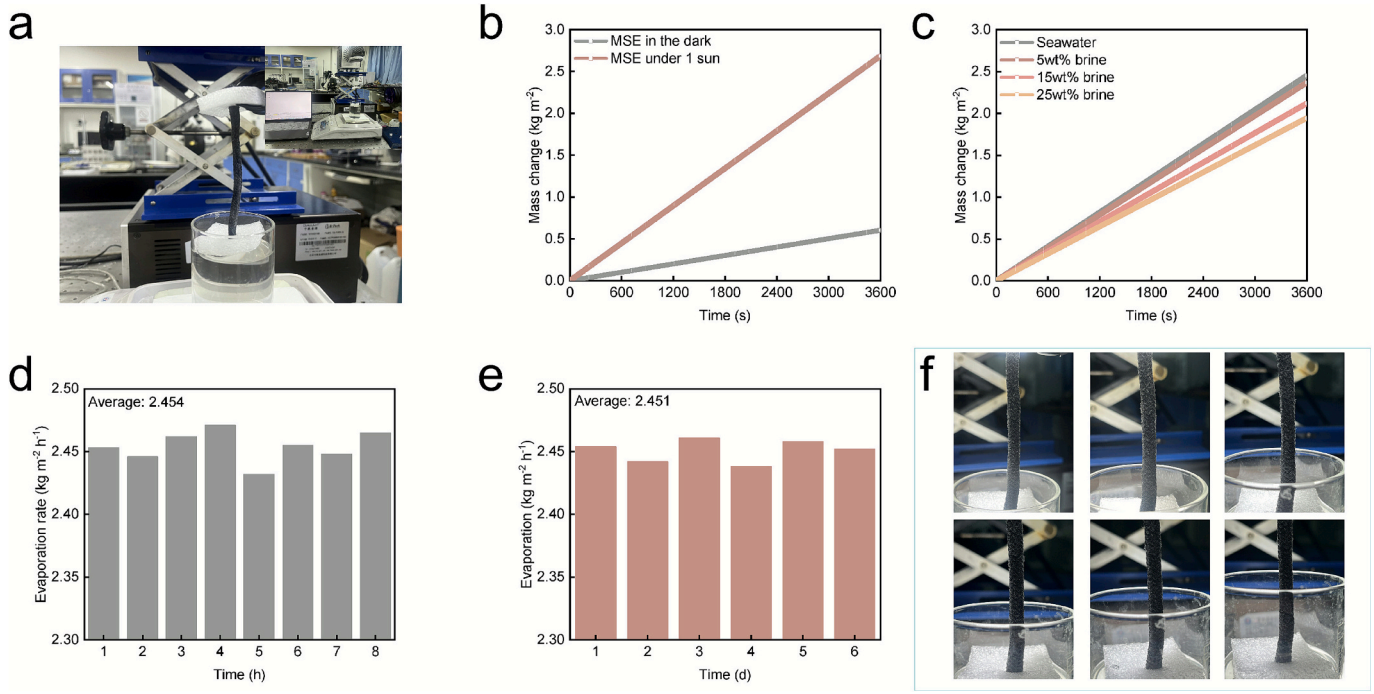


Fig. 3. Seawater Desalination and Long-term Stability. (a) The optical photograph of the indoor evaporation test. (b) The evaporation rate data of MSE for pure water in the dark and under 1 sun. (c) The evaporation rate data of MSE for seawater and brines with different concentrations under 1 sun. (d) The results of 8 h continuous seawater evaporation. (e) The results of 6 days continuous seawater evaporation. (f) The images of 6 days without salt crystallization.

the surface of MSE throughout the 6 days continuous seawater evaporation test, and this achievement is particularly remarkable. In the long-term operation of traditional seawater desalination evaporators, the accumulation of salt crystallization is often inevitable, and the occurrence of salt crystallization will seriously affect the evaporation efficiency of the evaporator and even cause equipment damage. However, MSE effectively circumvents this problem through its unique anti-salt mechanism, ensuring stability and high efficiency during long-term operation.

3.4. Numerical simulation and water-state during solar-driven evaporation

To verify the salt crystallization resistance of the MSE, numerical simulations of evaporation were conducted under illuminated and non-illuminated conditions. In dark conditions, the numerically predicted evaporator temperature is ~293 K (in good agreement with the experimental measurement of 19.45 °C), with the corresponding evaporation rate remaining low (Fig. 4a and Fig. 4b). Under 1-sun irradiation, the evaporator surface temperature increases to 323 K (matching the experimental 45.09 °C), while the evaporation rate rises significantly (Fig. 4c and Fig. 4d). For a 10 wt% NaCl solution, the numerically calculated salt flow speed is relatively high (Fig. 4e), and the local salt concentration remains substantially lower than the initial concentration (Fig. 4f)-validating the MSE's experimentally observed salt-rejection capability [44,45]. Further simulations of salt flow and concentration distributions in the water film additionally predict no salt crystallization during seawater evaporation, fully consistent with experimental results [46,47]. The MSE exhibits excellent pure water and seawater evaporation rates (Supplementary Table 2), outperforming most reported values in relevant literature and even exceeding the theoretical evaporation limit of ~1.47 $kg{\cdot}m^{-2}{\cdot}h^{-1}$ under 1-sun irradiation [48,47]. To elucidate this phenomenon (i.e., the evaporation rate surpassing the theoretical limit), the physical state of water confined in the evaporator was characterized; corresponding optical micrographs are shown in Fig. 5a (wetted state during active evaporation).

An isolated H_2O molecule possesses three fundamental normal vibrational modes, designated as $2A_1+B_1$: the A_1 symmetry species is associated with both the symmetric stretching vibration (3657 cm^{-1}) and bending vibration (1595 cm^{-1}), while the B_1 symmetry species corresponds to the antisymmetric stretching vibration (3756 cm^{-1}) [49,50]. Upon the formation of intermolecular hydrogen bonds, electron density redistributes across interacting orbitals, leading to the shortening of both H···O and O···O intermolecular distances [51]. This structural perturbation induces substantial reorganization of the hydrogen-bonding network confined within the porous scaffold of the Janus evaporator. Micro-Raman spectroscopy measurements (532 nm laser excitation) demonstrate that the broad O–H stretching band envelope (centered at ~3400 cm^{-1}) in bulk water can be readily deconvoluted into five discrete sub-bands—DDAA-OH (≈3226 cm^{-1}), DDA-OH (≈3573 cm^{-1}), DAA-OH (≈3005 cm^{-1}), DA-OH (≈3434 cm^{-1}), and Free-OH (≈3640 cm^{-1})—each corresponding to a distinct hydrogen-bond connectivity configuration (Fig. 5b). In bulk water, DDAA-OH and DA-OH species dominate the air–water interface (Fig. 5c). In contrast, the hydrogen-bonding network within the evaporator undergoes a pronounced transformation (Fig. 5d): the previously dominant DDAA-OH and DA-OH moieties are replaced by DDA-OH and Free-OH configurations (Fig. 5b: blue and gray spheres represent hydrogen and oxygen atoms, respectively), which exhibit lower energetic requirements [52,53]. Notably, this redistribution of hydrogen-bond configurations facilitates the formation of larger, lower-energy water clusters. Consequently, compared to bulk water, evaporation occurs primarily via the release of pre-formed water clusters-an effect that reduces the effective evaporation enthalpy.

Differential scanning calorimetry (DSC) was used to quantify the evaporation enthalpy of bulk water, yielding a value of 2440 $kJ{\cdot}kg^{-1}$ (Fig. S2). Dark-evaporation experiments showed that bulk water had an evaporation rate of 0.415 $kg{\cdot}m^{-2}{\cdot}h^{-1}$, while water confined in the solar evaporator exhibited a notably higher rate of 0.603 $kg{\cdot}m^{-2}{\cdot}h^{-1}$ (Fig. S3); this 31.2 % enhancement in evaporation rate corresponds to a reduction in evaporation enthalpy to approximately 1680 $kJ{\cdot}kg^{-1}$ [54,55]. Similarly, comparisons of dark evaporation rates between bulk

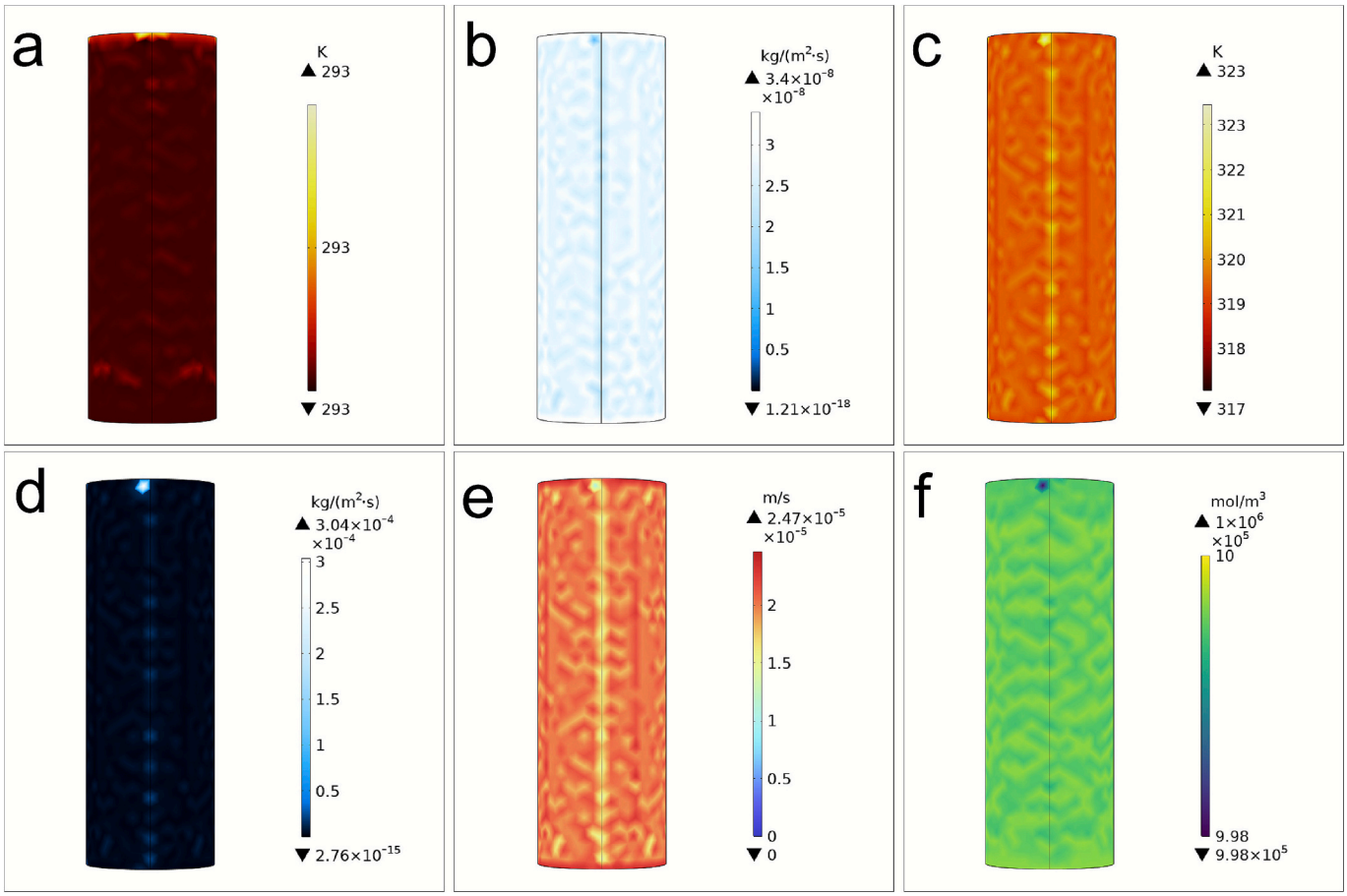


Fig. 4. Numerical Simulation of the Solar-Driven Evaporation Process. (a) Temperature distribution in the dark. (b) Evaporation rate in the dark. (c) Temperature distribution under 1 sun irradiation. (d) Evaporation rate under 1 sun irradiation. (e) Salt flow speed under 1 sun irradiation. (f) Salt concentration under 1 sun irradiation.

saline solutions (of varying concentrations) and water confined in the solar evaporator revealed an analogous trend, confirming that the MSE also reduces evaporation enthalpy when processing saline water (Fig. S4, Fig. S5 and Supplementary Table 3). Deconvolution of Raman spectra (Fig. 5e) indicated that the intermediate water-to-free water (IW/FW) ratio increased from 12.86 % (bulk water) to 15.73 % (water confined in the evaporator). The elevated population of intermediate water weakens the average hydrogen-bond strength in the water system, thereby lowering the enthalpy required for evaporation [56]. To further corroborate this enthalpy reduction, lithium ion (Li^+) tracer experiments were conducted. Condensates from direct evaporation showed constant Li^+ concentrations, whereas those from solar-driven evaporation exhibited Li^+ contents correlated with the initial Li^+ concentration of the feed solution. This observation suggests that Li^+ ions are transported within water clusters, which are preferentially transferred to the vapor phase (Fig. 5f). Collectively, these results provide independent experimental evidence that the effective evaporation enthalpy of water confined in the evaporator is significantly reduced [41,57].

3.5. Outdoor tests and freshwater collection

From the photo of the scaled-up MSE in Fig. 6a, it can be seen that this evaporator has good scalability, laying the foundation for large-scale seawater desalination and freshwater collection. Its large-scale structural design is beneficial for making full use of seawater resources to produce fresh water in practical application scenarios such as water-scarce coastal areas or offshore platforms. The photo in Fig. 6b, which shows the MSE assembled with a condenser into an outdoor freshwater collection device, visually presents the complete architecture of the freshwater collection system. All components work synergistically, closely integrating the seawater evaporation and steam condensation processes, providing hardware support for efficient freshwater collection. The photo in Fig. 6c, showing the rapid formation of droplets at the top of the condenser, further demonstrates the efficient coordination between the evaporation efficiency of MSE and the condensation effect of the condenser. Droplets can be observed to form in a very short time, which means that this device can quickly convert evaporated seawater into liquid fresh water, greatly increasing the speed of freshwater collection and meeting the demand for rapid access to fresh water in practical applications. The freshwater collection rate (Day 1) recorded in Fig. 6d and the daily freshwater collection (about 10.18 $L{\cdot}m^{-2}$) obtained from 7 days continuous recording in Fig. 6e fully demonstrate the stable production capacity of MSE in the actual outdoor environment (Fig. S6). The relatively stable daily freshwater collection indicates that this device is not significantly affected by daily fluctuations in environmental factors such as illumination and temperature, and can operate continuously and efficiently, providing a guarantee for long-term and stable freshwater supply.

In terms of the ion concentration comparison between seawater and the collected freshwater (Fig. 6f), a detailed analysis of sodium, magnesium, calcium, and potassium ions reveals the outstanding seawater purification ability of MSE. The Na^+ concentration in seawater is typically as high as about 10880 mg/L, while in the collected freshwater, it drops sharply to less than 3.5 mg/L, with a removal rate of over 99.8 %. The Mg^{2+} concentration in seawater is approximately 1290 mg/L and is reduced to less than 1.4 mg/L in freshwater, with a removal rate close to

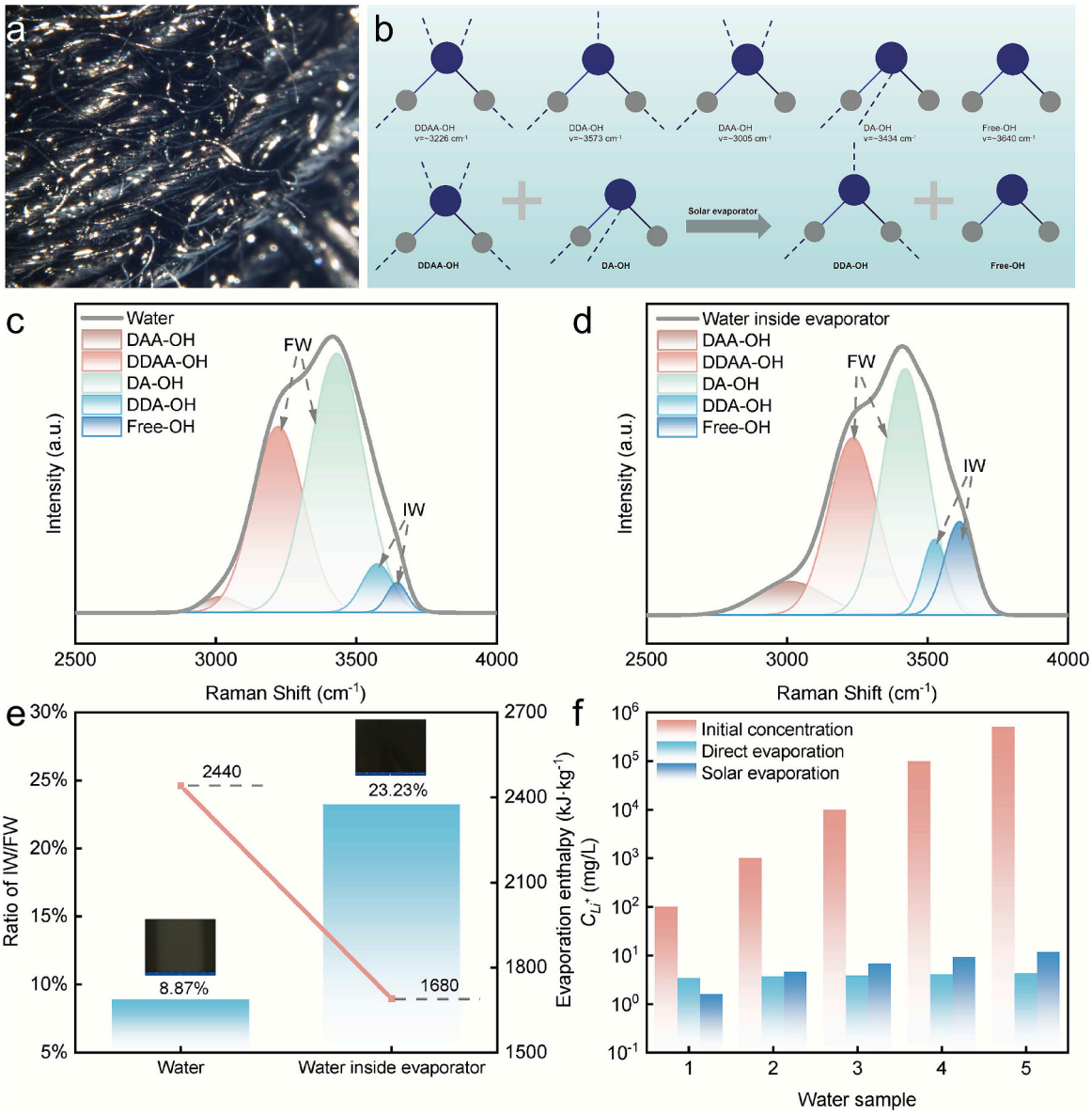


Fig. 5. Water-State During Evaporation. (a) Optical micrograph of the solar evaporator in an operationally wetted state (i.e., during active evaporation). (b) Schematic illustration of hydrogen-bonding network reorganization in water during the evaporation process. (c) Normalized Raman spectrum of bulk water. (d) Normalized Raman spectrum of water confined within the solar evaporator. (e) Changes in the ratio of intermediate water/free water and evaporation enthalpy. (f) Concentration changes of lithium ions in condensate collected by traditional evaporation and solar evaporation.

100 %. The Ca^{2+} concentration in seawater is around 410 mg/L and decreases to less than 0.5 mg/L in the collected freshwater, showing a remarkable removal rate as well. The K^{+} concentration in seawater is about 390 mg/L and is less than 0.4 mg/L in freshwater. Through the treatment of MSE, the concentrations of these ions are significantly reduced to extremely low levels. When comparing the ion concentrations of the collected freshwater with the drinking water standards of the World Health Organization (WHO), the results are encouraging. WHO stipulates that the upper limit of Na^{+} in drinking water is 200 mg/L, that of Mg^{2+} is 150 mg/L, that of Ca^{2+} is 200 mg/L, and that of K^{+} is 12 mg/L [58,59]. The ion concentration indicators of the freshwater collected by MSE are far below the WHO standards, which fully demonstrates the high quality of the produced freshwater, fully meeting the drinking requirements. More importantly, after the continuous evaporation tests, we examined the SEM images (Fig. S7), and no structural damage to the evaporator or salt deposits were observed. This achievement is of great significance as it means that MSE can provide a safe and reliable source of drinking water for areas lacking freshwater resources, effectively solving the drinking water problems of local residents. Looking to the future, MSE has broad application prospects in the field of outdoor freshwater collection. Further optimizing the device, such as improving its energy utilization efficiency, reducing operating costs, and enhancing its adaptability to seawater of different qualities, will help promote MSE from the experimental stage to a wider range of practical applications, providing practical solutions to the global water shortage problem.

3.6. *Economic analysis*

The PVA, GO, cotton fibers, and PS foam used in this evaporator are all conventional low-cost materials, with low unit prices for bulk procurement. Its preparation does not require high-temperature and high-pressure equipment, and its energy consumption is only 15 % of that of traditional thermal methods. During the operation phase, no chemical agents are added, leading to low maintenance costs. The detailed cost calculation equations are provided in Supplementary Note 2. Combined with a daily freshwater collection capacity of 10.18 $L{\cdot}m^{-2}$, the

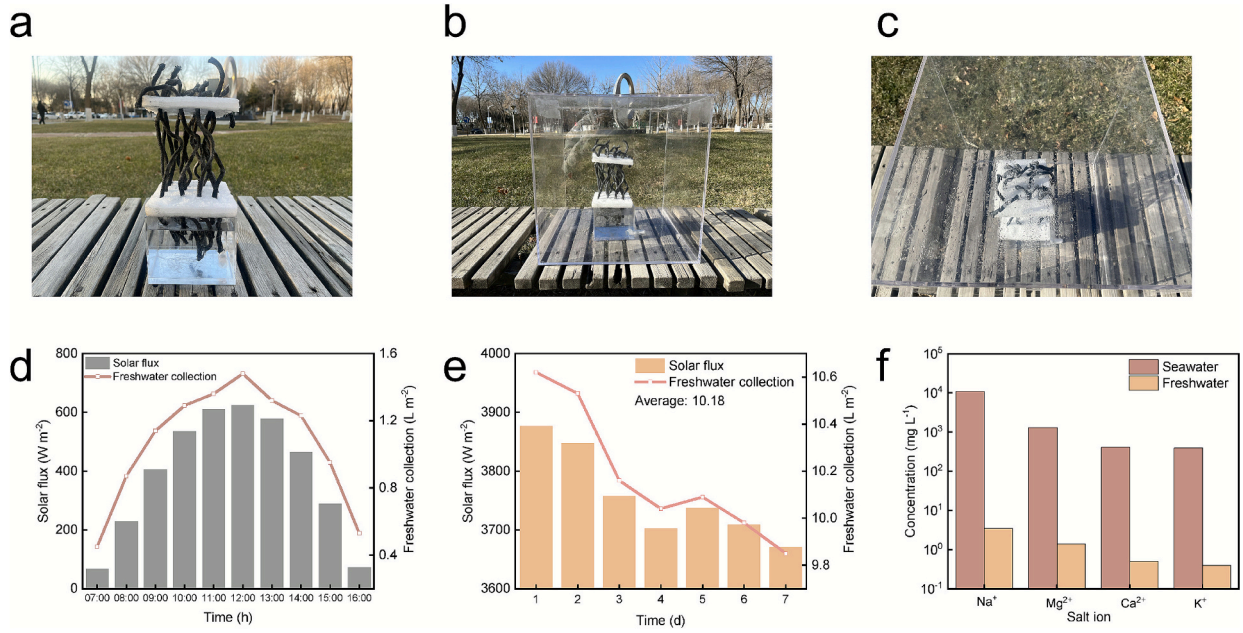


Fig. 6. Outdoor Tests and Freshwater Collection. (a) The photo of the scaled-up MSE. (b) The photo of the outdoor freshwater collection device. (c) The photo of rapid formation of droplets at the top of the condenser. (d) The 1-day freshwater collection. (e) The 7-days freshwater collection. (f) The salt ion concentration comparison between seawater and freshwater.

converted unit cost of freshwater is approximately 0.074 USD/L, which is significantly lower than that of traditional membrane methods (0.17–0.26 USD/L) and thermal methods (0.29–0.50 USD/L). Additionally, the estimated service life of the equipment is over 3 years, showing obvious long-term economic advantages. Based on the characteristic that the equipment's energy consumption is only 15 % of that of traditional thermal methods, and taking the freshwater output per unit energy input as the core indicator, it is calculated that each kilowatt-hour (kWh) of electrical energy can produce approximately 17.3 L (L) of freshwater, corresponding to an energy cost of about 0.004 USD/L (calculated based on an industrial electricity price of 0.086 USD/kWh. This cost is significantly lower than that of traditional thermal methods (0.026 USD/L) and membrane methods (0.011 USD/L), demonstrating the synergistic advantages of energy utilization and economic cost. The main exergy loss links are identified as photothermal conversion (with exergy loss accounting for 32 %) and heat transfer (with exergy loss accounting for 21 %). Through cost coupling calculation, the economic cost corresponding to the aforementioned exergy losses accounts for 45 % of the total operating cost. However, in this study, the photothermal conversion efficiency is improved by the PVA-GO coating, and heat loss is reduced by polystyrene foam, which reduces the economic cost of exergy loss by 18 %. This further verifies the exergo-economic rationality of the technical scheme.

4. Conclusion

This study presents an interfacial evaporator inspired by marine seeding. Polyvinyl alcohol (PVA) and graphene oxide (GO) not only harden cotton fibers but also endow the composite with excellent wetting properties and photothermal conversion performance. In terms of seawater desalination efficiency, the marine seeding evaporator (MSE) exhibits robust treatment capabilities for brines of various concentrations and real seawater. During a 6-day continuous seawater evaporation test, it maintains a stable evaporation rate of 2.451 $kg{\cdot}m^{-2}{\cdot}h^{-1}$ without salt crystallization, verifying its operational reliability. The high evaporation efficiency stems from reduced water evaporation enthalpy, which is attributed to the altered water state within the evaporator. Furthermore, utilizing low-cost and readily available materials enables efficient freshwater collection, with a unit cost of ~0.074 USD/L-lower than traditional reverse osmosis (RO) and multi-effect distillation (MED) technologies (0.17–0.50 USD/L), offering complementary value for decentralized scenarios. Outdoor tests confirm that the collected freshwater meets WHO drinking water standards, with all salt ion concentrations well below the specified limits. While this work provides a promising integrated interfacial evaporation solution to promote lab-to-practical large-scale application and alleviate global water scarcity, future research will address potential challenges such as biofouling beyond 6-day operation and performance under hypersaline conditions (>25 wt%).

CRediT authorship contribution statement

Xinzhe Liu: Writing – original draft, Software, Methodology, Investigation, Conceptualization. **Ting Chen:** Writing – review & editing, Supervision, Investigation. **Tiezhi Wang:** Supervision, Investigation. **Jinliang Xu:** Writing – review & editing, Supervision, Investigation. **Ying He:** Methodology, Investigation. **Guohua Liu:** Writing – review & editing, Supervision, Methodology, Investigation, Funding acquisition, Conceptualization.

Declaration of competing interest

The authors declare that there are no competing interests or personal relationships that could have influenced the research reported in this paper.

Acknowledgements

This research was supported by the Natural Science Foundation of China (52376143, 52306086).

Appendix A. Supplementary data

Supplementary data to this article can be found online at https://doi.org/10.1016/j.solener.2026.114327.

Data availability

The data supporting the findings are presented in the main text. Raw data are available from the corresponding author upon reasonable request.

References

[1] M. Salehi, Global water shortage and potable water safety; Today's concern and tomorrow's crisis, Environ. Int. (2022) 158.
[2] E. Savelli, M. Mazzoleni, G. Di Baldassarre, H. Cloke, M. Rusca, Urban water crises driven by elites' unsustainable consumption, Nat. Sustainability 6 (8) (2023) 929–940.
[3] O. Shumilova, K. Tockner, A. Sukhodolov, V. Khilchevskyi, L. De Meester, S. Stepanenko, G. Trokhymenko, J.A. Hernandez-Agueero, P. Gleick, Impact of the Russia-Ukraine armed conflict on water resources and water infrastructure, Nat. Sustainab. 6 (5) (2023) 578–586.
[4] M.E. Hauer, S.A. Jacobs, S.A. Kulp, Climate migration amplifies demographic change and population aging, Proc. Natl. Acad. Sci. USA 121 (3) (2024).
[5] R. Trancoso, J. Syktus, R.P. Allan, J. Croke, O. Hoegh-Guldberg, R. Chadwick, Significantly wetter or drier future conditions for one to two thirds of the world's population, Nat. Commun. 15 (1) (2024).
[6] S.I. Higgins, T. Conradi, E. Muhoko, Shifts in vegetation activity of terrestrial ecosystems attributable to climate trends, Nat. Geosci. 16 (2) (2023) 147-+.
[7] A.K. Priya, M. Muruganandam, S. Rajamanickam, S. Sivarethinamohan, M.K. R. Gaddam, P. Velusamy, R. Gomathi, G. Ravindiran, T.R. Gurugubelli, S. K. Muniasamy, Impact of climate change and anthropogenic activities on aquatic ecosystem - a review, Environ. Res. 238 (2023).
[8] P.Y. Li, J.H. Wu, Drinking water quality and public health, Exp. Health 11 (2) (2019) 73–79.
[9] M.S. Mauter, I. Zucker, F. Perreault, J.R. Werber, J.H. Kim, M. Elimelech, The role of nanotechnology in tackling global water challenges, Nat. Sustainability 1 (4) (2018) 166–175.
[10] S.S. Lin, H.Y. Zhao, L.P. Zhu, T. He, S.F. Chen, C.J. Gao, L. Zhang, Seawater desalination technology and engineering in China: a review, Desalination 498 (2021).
[11] Y.H. Cai, J.F. Wu, S.Q. Shi, J.Z. Li, K.H. Kim, Advances in desalination technology and its environmental and economic assessment, J. Clean. Prod. 397 (2023).
[12] J. Eke, A. Yusuf, A. Giwa, A. Sodiq, The global status of desalination: an assessment of current desalination technologies, plants and capacity, Desalination 495 (2020).
[13] G. Amy, N. Ghaffour, Z.Y. Li, L. Francis, R.V. Linares, T. Missimer, S. Lattemann, Membrane-based seawater desalination: present and future prospects, Desalination 401 (2017) 16–21.
[14] A. Panagopoulos, K.J. Haralambous, Environmental impacts of desalination and brine treatment - challenges and mitigation measures, Mar. Pollut. Bull. 161 (2020).
[15] D. Li, Y.S. Yan, H.T. Wang, Recent advances in polymer and polymer composite membranes for reverse and forward osmosis processes, Prog. Polym. Sci. 61 (2016) 104–155.
[16] Y.J. Yao, P.X. Zhang, C. Jiang, R.M. DuChanois, X. Zhang, M. Elimelech, High performance polyester reverse osmosis desalination membrane with chlorine resistance, Nat. Sustainability 4 (2) (2021) 138–146.
[17] F.E. Ahmed, A. Khalil, N. Hilal, Emerging desalination technologies: current status, challenges and future trends, Desalination 517 (2021).
[18] C. Skuse, A. Gallego-Schmid, A. Azapagic, P. Gorgojo, Can emerging membrane-based desalination technologies replace reverse osmosis? Desalination 500 (2021).
[19] W.X. Liang, J.T. Han, Y. Ge, W.C. Zhu, J.W. Yang, W. Lv, C.H. Liu, Investigation on combining multi-effect distillation and double-effect absorption refrigeration cycle to recover exhaust heat of SOFC-GT system, Energy Conv. Manage. 301 (2024).
[20] J.H. Yu, C.X. Wang, S. Liu, S. Yang, X.M. Du, S. Liu, C.X. Shao, H.J. Kong, B. L. Wang, T. Wu, C.W. Li, Solid waste-derived solar desalination devices: Enhanced efficiency in water vapor generation and diffusion, Chem. Eng. J. 485 (2024).
[21] M. Al-Obaidi, A.A. Alsarayreh, F.L. Rashid, M.T. Sowgath, S. Alsadaie, A. Ruiz-García, M. Khayet, N. Ghaffour, I.M. Mujtaba, Hybrid membrane and thermal seawater desalination processes powered by fossil fuels: a comprehensive review, future challenges and prospects, Desalination 583 (2024).
[22] M.T. Ali, H.E.S. Fath, P.R. Armstrong, A comprehensive techno-economical review of indirect solar desalination, Renew. Sustain. Energy Rev. 15 (8) (2011) 4187–4199.
[23] S.W. Sharshir, M.M. Elsayad, M. Ismail, A.W. Kandeal, An innovative multi-stage flash distillation unit integrated with evacuate tubes water heater and water mists: a (4E/2S) estimation, Energy Conv. Manage. 327 (2025).
[24] S. Liu, S.T. Li, M. Lin, Understanding interfacial properties for enhanced solar evaporation devices: from geometrical to physical interfaces, ACS Energy Lett. (2023) 1680–1687.
[25] P. Tao, G. Ni, C.Y. Song, W. Shang, J.B. Wu, J. Zhu, G. Chen, T. Deng, Solar-driven interfacial evaporation, Nat. Energy 3 (12) (2018) 1031–1041.
[26] K.Y. Xu, C.B. Wang, Z.T. Li, S.M. Wu, J.L. Wang, Salt mitigation strategies of solar-driven interfacial desalination, Adv. Funct. Mater. 31 (8) (2021).
[27] Y.X. Zhang, T. Xiong, D.K. Nandakumar, S.C. Tan, Structure architecting for salt-rejecting solar interfacial desalination to achieve high-performance evaporation with in situ energy generation, Adv. Sci. 7 (9) (2020).
[28] L.L. Zhu, M.M. Gao, C.K.N. Peh, G.W. Ho, Recent progress in solar-driven interfacial water evaporation: Advanced designs and applications, Nano Energy 57 (2019) 507–518.
[29] Z.Y. Li, X. Ma, D.K. Chen, X.Y. Wan, X.B. Wang, Z. Fang, X.S. Peng, Polyaniline-coated MOFs nanorod arrays for efficient evaporation-driven electricity generation and solar steam desalination, Adv. Sci. 8 (7) (2021).
[30] Y. Lu, D.Q. Fan, Z.Y. Shen, H. Zhang, H.L. Xu, X.F. Yang, Design and performance boost of a MOF-functionalized-wood solar evaporator through tuning the hydrogen-bonding interactions, Nano Energy (2022) 95.
[31] L.F. Cui, C.W. Ma, P.F. Wang, H.A. Che, H.L. Xu, Y.H. Ao, Rationally constructing a 3D bifunctional solar evaporator for high-performance water evaporation coupled with pollutants degradation, Appl. Catal. B-Environ. Energy 337 (2023).
[32] L.X. Li, J.P. Zhang, Highly salt-resistant and all-weather solar-driven interfacial evaporators with photothermal and electrothermal effects based on Janus graphene@silicone sponges, Nano Energy 81 (2021).
[33] H.R. Li, Z. Yan, Y. Li, W.P. Hong, Latest development in salt removal from solar-driven interfacial saline water evaporators: Advanced strategies and challenges, Water Res. 177 (2020).
[34] B.L. Zeng, T. Kumar, H.Y. Wu, S. Stark, H. Hamza, H.Y. Zhao, H.L. Xu, X.H. Zhang, Evolution of morphology and distribution of salt crystals on a photothermal layer during solar interfacial evaporation, Langmuir 39 (41) (2023) 14737–14747.
[35] D.X. Wu, M.H. Cheng, X.S. Zhang, Synergistic modification of fabric evaporator by polydopamine and carbon nanoparticles for efficient and scalable solar steam generation, Appl. Therm. Eng. 244 (2024).
[36] J.J. Hu, Y. Sun, Z.X. Liu, B. Zhu, L.S. Zhang, N. Xu, M.F. Zhu, J. Zhu, Z.G. Chen, Photothermal fabrics for solar-driven seawater desalination, Prog. Mater. Sci. 150 (2025).
[37] Q.Q. Liu, X.J. Liu, G. Chen, P. Feng, Y.C. Xiong, M. An, C. Shao, X.F. Zhu, R. Z. Wang, J.S. Sun, J.S. Sun, C.F. Guo, S.Y. Bi, S.H. Li, A robust and low-cost blended-fiber-based evaporator with high efficiency for solar desalination, Desalination 583 (2024).
[38] X.H. Wu, D. Lin, H.F. Zhou, L. Han, J.Y. Li, H.J. Ma, B.W. Zhang, Salt crystallization on porous asymmetrical graphene oxide-based photothermal hydrogel-fabric unexpectedly enables continuous solar-powered hypersaline water distillation, Carbon 233 (2025).
[39] L.M. Zhao, L.W. Zhang, Z.P. Yang, T. Zhou, P. Cao, L. Chen, Y.Y. Zhang, T.T. Qin, Z. Z. Yong, K.J. Wu, Q.W. Li, Twisted integration of high-efficiency photothermal/water-transported yarns for boosting solar-powered fabric evaporator, Chem. Eng. J. 490 (2024).
[40] H.F. Zhou, L. Han, M. Yang, X.H. Wu, J.Y. Li, H.J. Ma, B.W. Zhang, Architecting Janus hydrogel-fabric coupled evaporator for eliminating salt accumulation and highly efficient solar-driven brine desalination, Desalination 556 (2023).
[41] Z.X. Liu, Z. Zhou, N.Y. Wu, R.Q. Zhang, B. Zhu, H. Jin, Y.M. Zhang, M.F. Zhu, Z. G. Chen, Hierarchical photothermal fabrics with low evaporation enthalpy as heliotropic evaporators for efficient, continuous, salt-free desalination, Acs Nano 15 (8) (2021) 13007–13018.
[42] Q.M. Sun, M. Sun, L.Y. Yang, Y. Gao, X.H. Zhou, L. Lyu, C.Y. Wei, Novel fabric-based 3D photothermal evaporator with advanced light-harvesting and thermal management design, Desalination 573 (2024).
[43] Y.Q. Huang, P.J. Zhong, N.N. Zhu, Y.Y. Li, Z. Xiao, K.Y. Han, B.B. Xu, S.Q. Xu, G. X. Bai, 3D reconfigurable hydroxylated carbon nanotubes-based water evaporators with long-distance transportation for continuous vapor generation, Chem. Eng. J. 500 (2024).
[44] L. Wu, Z.C. Dong, Z.R. Cai, T. Ganapathy, N.X. Fang, C.X. Li, C.L. Yu, Y. Zhang, Y. L. Song, Highly efficient three-dimensional solar evaporator for high salinity desalination by localized crystallization, Nat. Commun. 11 (1) (2020).
[45] M.M. Zou, Y. Zhang, Z.R. Cai, C.X. Li, Z.Y. Sun, C.L. Yu, Z.C. Dong, L. Wu, Y. L. Song, 3D printing a biomimetic bridge-arch solar evaporator for eliminating salt accumulation with desalination and agricultural applications, Adv. Mater. 33 (34) (2021).
[46] X.Z. Liu, Q.Y. Liu, Z. Liu, G.H. Liu, 3D printing cup evaporator with open architecture for seawater desalination, Chem. Eng. J. 505 (2025).
[47] F. Nawaz, Y.W. Yang, Q. Zhao, Y.L. Mo, Z.H. Jiang, J.H. Wu, Y.H. Liu, B.W. Liu, B. W. Gao, W.X. Que, Can the interfacial solar vapor generation performance be really "beyond" theoretical limit? Adv. Energy Mater. 14 (22) (2024).
[48] C.K. Du, X.P. Zhao, X. Qian, C.L. Huang, R.G. Yang, Heat-localized solar evaporation: Transport processes and applications, Nano Energy 107 (2023).
[49] Y.H. Wang, S.S. Zheng, W.M. Yang, R.Y. Zhou, Q.F. He, P. Radjenovic, J.C. Dong, S. N. Li, J.X. Zheng, Z.L. Yang, G. Attard, F. Pan, Z.Q. Tian, J.F. Li, In situ Raman spectroscopy reveals the structure and dissociation of interfacial water, Nature 600 (7887) (2021) 81-+.
[50] F. Zhao, Y.H. Guo, X.Y. Zhou, W. Shi, G.H. Yu, Materials for solar-powered water evaporation, Nat. Rev. Mater. 5 (5) (2020) 388–401.
[51] F. Perakis, L. De Marco, A. Shalit, F.J. Tang, Z.R. Kann, T.D. Kühne, R. Torre, M. Bonn, Y. Nagata, Vibrational spectroscopy and dynamics of water, Chem. Rev. 116 (13) (2016) 7590–7607.
[52] X.M. Geng, P. Yang, Y.F. Wan, How to reduce enthalpy in the interfacial solar water generation system for enhancing efficiency? Nano Energy 123 (2024).
[53] S.C. Singh, M. ElKabbash, Z.L. Li, X.H. Li, B. Regmi, M. Madsen, S.A. Jalil, Z. B. Zhan, J.H. Zhang, C.L. Guo, Solar-trackable super-wicking black metal panel for photothermal water sanitation, Nat. Sustainab. 3 (11) (2020) 938-+.
[54] J.M. Sun, S.Y. Zhao, X.S. Wang, W.Q. Kong, W. Li, S.F. Wang, S.X. Liu, S.X. Nie, Minimizing enthalpy of evaporation in solar steam generation: an emerging strategy beyond theoretical evaporation limitation, Mater. Today 80 (2024) 619–647.

[55] W.Q. Wang, X.P. Gao, J. Chen, C. Lu, Q.C. Zhang, Y.Z. Li, R.T. Zhang, D.H. Yao, X. C. Pang, All-biobased porous aerogels with low evaporation enthalpy for efficient solar interfacial evaporation, Sep. Purif. Technol. 358 (2025).
[56] A. Caratenuto, Y. Zheng, Critical assessment of water enthalpy characterization through dark environment evaporation, Sci. Adv. 10 (38) (2024).
[57] Z. Yu, R.N. Gu, Y. Tian, P.F. Xie, B.C. Jin, S.A. Cheng, Enhanced interfacial solar evaporation through formation of micro-meniscuses and microdroplets to reduce evaporation enthalpy, Adv. Funct. Mater. 32 (17) (2022).
[58] Z. Yu, Y.Q. Su, R.A. Gu, W. Wu, Y.X. Li, S.A. Cheng, Micro-nano water film enabled high-performance interfacial solar evaporation, Nano-Micro Letters 15 (1) (2023).
[59] L. Zhang, J. Liu, L.B. Yang, Z.J. Yu, J.B. Chen, H.Q. Chu, Y.L. Zhang, X.F. Zhou, Interfacial solar evaporation toward efficient recovery of clean water and concentration of nutrients from urine with polypyrrole-based photothermal conversion films, Resour. Conserv. Recycl. 188 (2023).